Catena 174 (2019) 478–489

Contents lists available at ScienceDirect

Catena

journal homepage: www.elsevier.com/locate/catena

UAV based soil moisture remote sensing in a karst mountainous catchment

Wei Luo[a,b], Xianli Xu[a,*], Wen Liu[c], Meixian Liu[a], Zhenwei Li[a], Tao Peng[d,e], Chaohao Xu[a,b], Yaohua Zhang[a,b], Rongfei Zhang[a,b]

[a] Huanjiang Observation and Research Station for Karst Ecosystem, Key Laboratory for Agro-ecological Processes in Subtropical Region, Institute of Subtropical Agriculture, Chinese Academy of Sciences, Changsha 410125, Hunan, China
[b] University of Chinese Academy of Sciences, Beijing 100049, China
[c] College of Resources and Environmental Sciences, Hunan Normal University, Changsha 410081, China
[d] State Key Laboratory of Environmental Geochemistry, Institute of Geochemistry, Chinese Academy of Sciences, Guiyang, Guizhou 550002, China
[e] Puding Karst Ecosystem Research Station, Puding, Guizhou, 562100, China

ARTICLE INFO

Keywords:
Earth critical zone
Ecohydrology
Landscape ecology
UAV photogrammetry
Soil hydrology

ABSTRACT

Spatial distribution of soil moisture (SM) is a prerequisite for research and management of agriculture and ecology. However, it is still a challenge to retrieve SM data in highly heterogeneous landscapes. By investigating environmental factors (soil, vegetation and topography) and comparing different remote sensing sources (Landsat-8, Radarsat-2, ASTER Global Digital Elevation Model (DEM) V002 (ASTGTM2), unmanned aerial vehicle (UAV)) for karst mountainous catchments of southwest China, this study identified key controlling factors on the spatial distribution of SM and built a remote sensing model for SM estimation in highly heterogeneous landscapes. Results showed that vegetation type (35.7%), aspect (7.7%), height index (4.2%), soil bulk density (3.3%), soil total nitrogen (3.1%), aspect interact with vegetation type (3.4%) and soil total phosphorous (1.3%) totally explained 58.8% of the SM variability. The correlations between SM and topographic derivatives varied with DEM resolutions (1–50 m), and generally reached their highest values at 7 m for height index, slope gradient, and aspect, 16 m for flow accumulation and topographic wetness index, and 43 m for curvature. Partial least-squares regression analysis showed that optical and infrared bands from Landsat-8 and topographic derivatives from UAV photogrammetry DEM were more strongly correlated with SM than other datasets. An empirical model ($SM = 9.27 * 10^{-2} HI - 1.82 * 10^{-5} B5 + 0.519$) with only height index and B5 band from Landsat-8 as inputs is proposed, as it shows acceptable performance ($R^2 = 0.36$; RMSE = 0.076). The results of this study provide useful information for SM remote sensing in karst mountainous area and similar heterogeneous landscapes.

1. Introduction

Soil moisture (SM) is a key factor affecting land surface fluxes of water and energy (Seneviratne et al., 2010). Therefore, monitoring of SM is necessary for agriculture development and ecosystem management. Compared to conventional techniques, remote sensing methods can rapidly obtain SM information on a regional scale, and therefore are becoming widely used in various hydrological and meteorological fields (Jackson et al., 2009; Jung et al., 2010; Kustas and Norman, 2009). SM remote sensing methods include optical sensing (Chang et al., 2001; Peng et al., 2013), synergistic methods of optical sensing with thermal infrared observations (Carlson, 2007) and microwave remote sensing methods (Kornelsen and Coulibaly, 2013). However, such models often perform poorly in heterogeneous landscapes (Fan et al., 2015; Feng et al., 2015; Vivoni et al., 2008a; Wagner et al., 2003). As a typical heterogeneous landscape, karst landform represents about 10% of the earth's land surface (http://geography.about.com/od/physicalgeography/a/karst.htm) and plays an important role in water supply for human society (Hartmann et al., 2014). Meanwhile, this region is facing severe environmental challenge such as extreme climate events and degradation (Liu et al., 2014; Liu et al., 2016). Hence, knowledge of the SM variation and estimation in such regions are essential for ecological protection and water resources management. As a result, there is an urgent need to develop specific models for karst landscapes.

As pointed in previous studies, soil moisture is affected by complex

* Corresponding author.
E-mail addresses: 2009301610278@whu.edu.cn (W. Luo), xianlixu@isa.ac.cn (X. Xu), liumeixian@isa.ac.cn (M. Liu), lizhenwei337@isa.ac.cn (Z. Li), pengtao@mail.gyig.ac.cn (T. Peng).

https://doi.org/10.1016/j.catena.2018.11.017
Received 22 March 2018; Received in revised form 8 November 2018; Accepted 14 November 2018
Available online 05 December 2018
0341-8162/

interactions from many factors including meteorology (rainfall, temperature, wind speed, radiation), soil properties, vegetation, and topography (Beldring et al., 1999; Burt and Butcher, 1985; Chen et al., 2010; Li et al., 2014a; Ma et al., 2004; Vivoni et al., 2008b; Zhang et al., 2016). In highly diverse landscapes, complex topography plays a key role in the spatial distribution of SM, since topography determines the lateral transport of SM to some extent (Appels et al., 2011; Baldwin et al., 2017). As expected, models that include topographic information seem to be more efficient at SM monitoring (Houser et al., 1998; Moore et al., 1991; Wilson et al., 2005).

Digital Elevation Model (DEM) is a data source for topographic variables. Previous research has demonstrated that modeled surface hydrological attributes are sensitive to DEM grid resolution and DEM sources (Penizek et al., 2016; Sørensen and Seibert, 2007; Thomas et al., 2017; Woodrow et al., 2016). The raster resolution can directly influence the computation of topographic derivatives and the details of morphological description of a specific area (Ariza-Villaverde et al., 2015; Thompson et al., 2000). However, the general expectation that the finest resolution delivers the best results is not always valid (Smith et al., 2006; Sørensen and Seibert, 2007). In some cases, the optimal resolution is driven by the characteristics of the mapped terrain features (Napieralski and Nalepa, 2010). In highly heterogeneous landscapes, for example, the karst landscape in southwest China which is characterized by complex terrain with steep hillslopes and deep depressions, the resolution of the topographic derivatives may be important for SM estimation. However, few studies have focused on this issue. Previous studies have researched the variability of SM in karst areas (Chen et al., 2010; Chen et al., 2009; Liu et al., 2017; Ries et al., 2015; Zhang et al., 2011), but few of these studies have been at a catchment scale, and none of them have used remote sensing techniques.

Therefore, our study aims to explore 1) key controlling factors on spatial distribution of SM in karst catchments, 2) key remote sensing data sources and key variables for estimating spatial distribution of SM, and 3) an efficient empirical model for estimating spatial distribution of SM in karst catchments.

2. Materials and methods

2.1. Study area

The Chenqi (1.3 km^2) and Dengzhanhe (1.8 km^2) catchments in southwest China, were selected for this study (Fig. 1). The two catchments are in a region characterized by subtropical monsoon climate. Dengzhanhe catchment had steeper and longer hillslopes and sparser vegetation community than Chenqi catchment. The mean annual temperature is 20.1 °C. July has the highest average monthly temperature, and January has the lowest. Annual precipitation is 1140 mm, with a distinct wet season in the summer and a dry season in winter. Average monthly humidity ranges from 74 to 78%. The elevation of the study region ranges from 1320 to 1520 m. With the typical cone karst and cockpit karst geomorphology, the catchments are characterized by sinkholes formed by the dissolution of soluble rock. Soils are rocky and thin. The gaps, fissures and channels in the epikarst caused rapid transport of surface water to groundwater (White, 2002).

2.2. Procedure

The workflow used in this study is shown in Fig. 2. It consisted of four steps: a) preprocessing of data sets; b) determination of optimal resolutions for topographic derivatives; c) comparison of remote sensing variables for SM retrieval; and d) modeling and validation for SM estimation. Step a will be introduced in Sections 2.3 and 2.4, while, step b, c and d will be detailed in Sections 2.6, 2.7 and 2.8, respectively.

2.3. Field experiments

The study site encompassed two catchments; the Dengzhanhe watershed and the Chenqi watershed (Fig. 1). On March 14th, 2016, a total of 222 soil samples from six vegetation types (woodland (n = 38), wood-shrubland (n = 25), shrubland (n = 30), grassland (n = 63), abandoned land (n = 36) and farmland (n = 30)) were collected (Fig. 1). March 14th was in the last days of dry period at the study site. And in the last winter (December 1st, 2015 to March 14th, 2016), totally 6 rainfall events brought 66.6 mm precipitation. Since Liu et al. (2014) pointed out that southwestern China is experiencing more frequent drought, we chose March 14th as our sampling date and attempt to investigate the SM variation after continuous drought. The sampling strategy considered the spatial distribution, vegetation and topography to ensure that the sampling points were well distributed. The gaps of sampling points were at least 30 m, and each sampling points were located at the center of a certain vegetation community with the area of at least 900 m^2, thus made the sampling data represent the sampling points as possible. Surface soil samples (from 0 to 5 cm depth) were collected. Soil moisture content and bulk density was measured by collecting soil in a steel ring (volume: 100 cm^3) and weighing its dry-mass after oven drying as 105 °C (ISO, 1998). Soil textures were determined using a laser particle analyzer (Master sizer 2000). The bare rock coverage was visually estimated by metric card. The chemical properties measured were total nitrogen, total phosphorus and SOC using standard methods (combustion with an elemental analyzer, double acid extraction method and wet oxidation method, respectively) (Pansu and Gautheyrou, 2006).

At the same time, UAV photogrammetry was processed to generate a high-resolution (0.12 m) DEM of these two watersheds. We took 284 images by a UAV (DJI Phantom 3 professional edition, https://www.dji.com) at 500 m relative height to the ground. Then, aerial triangulation was done in software of Context Capture Master 4.0.0 (https://www.bentley.com). The DEM was georeferenced (Harwin and Lucieer, 2012; Niethammer et al., 2012) by 8 ground control points which were measured with the total station. Moreover, we did a direct georeferencing (D'Oleire-Oltmanns et al., 2012) using the navigation-grade GPS on-board the UAV to figure out that, is the precision of this simplest and least accurate georeferencing method qualified to hydrological research.

2.4. Satellite remote sensing data

The Landsat-8 (March 20th, 2016), Radarsat-2 (March 14th, 2016), and ASTGTM2 were used for this research. The Landsat-8 (30 m resolution) provides 9 individual bands from 433 to 2300 nm and a normalized difference vegetation index (NDVI). Radarsat-2 (10 m resolution) provides C band microwave backscatter information under four polarization patterns, including the horizontal- horizontal (HH), horizontal-vertical (HV), vertical-horizontal (VH) and vertical-vertical (VV) (Table 1). The preprocessing of Radarsat-2 was performed using ENVI SARscape 5.1 (http://www.harrisgeospatial.com). The ASTGTM2 is popular topographic data used in previous research and provides DEM of 30 m resolution (Suwandana et al., 2012).

2.5. Major controlling factors of soil moisture

We created a generalized linear model (Nelder and Wedderburn, 1972) of the SM to environmental factors, using stepwise regression (Bendel and Afifi, 1977) to investigate the major controlling factors of SM. The environmental factors contained vegetation type, soil properties and topographic factors, detailed in Table 2. The algorithms used forward and backward stepwise regression to determine a final model. At each step, the method searched for terms to add or remove from the model based on criterion argument. The criterion argument was calculated by *p*-value and *F*-statistic which tested models with and without

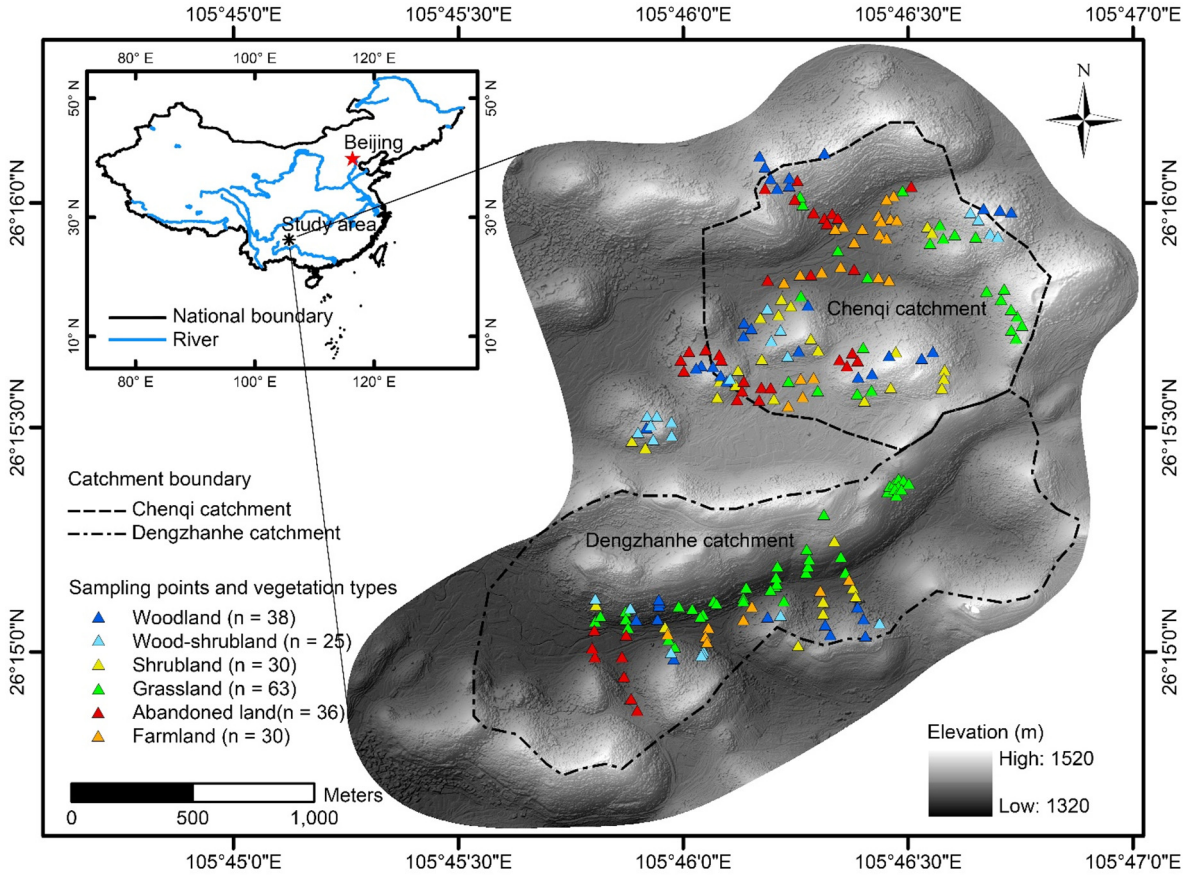

Fig. 1. Study area and sampling points. 222 sampling points were well distributed in Chenqi and Dengzhanhe catchments, southwest China.

a potential term at each step. If a term was not momentarily in the model, the null hypothesis was that the term would have a zero coefficient if added to the model. If there was sufficient evidence to reject the null hypothesis, the term was added to the model. Conversely, if a term was momentarily in the model, the null hypothesis was that the term had a zero coefficient. If there was insufficient evidence to reject the null hypothesis, the term was removed from the model. The method terminated when no single step improves the model. The terms included in the initial model and the order in which terms are moved in explained the major controlling factors of soil moisture.

2.6. Optimal resolutions for topographic derivatives

The 0.12 m UAV photogrammetry DEM was resampled to generate 50 DEMs with different resolutions ranging from 1 m to 50 m (1 m intervals). Based on these 50 DEMs and the ASTGTM2 (30 m), 8 topographic derivatives, including height index (HI), slope gradient (SLOPE), aspect from north to south (ASPECT), surface curvature (SURF), plan curvature (PLAN), profile curvature (PROF), flow accumulation (FACC) and topographic wetness index (TWI) were calculated for each sample site using ArcGIS 10.3 (https://www.esri.com). Descriptions of these topographic derivatives are shown in Table 1.

Pearson correlation analysis between SM and topographic derivatives with different resolutions was conducted. The resolution at which the correlation reached to its highest (absolute) value was selected as the optimal resolution. To illustrate the advantage of UAV photogrammetry and potential on hydrological research. We compared UAV photogrammetry DEMs with the ASTGTM2 DEM, the relationship between SM and topographic derivatives based on ASTGTM2 were also investigated

2.7. Importance of remote sensing variables for SM estimation

A partial least-squares regression (PLSR) technique (Vinzi et al., 2010) was applied to select predictors for SM estimation. Potential predictors were divided into four groups (Landsat-8, Radarsat-2, ASTGTM2, UAV) which contained information from 433 nm to 2300 nm wavelengths, microwave backscatter coefficients and topographic derivatives. PLSR is a powerful technique to deal with data that contain correlated predictor variables, and have advantages over similar analysis methods (such as stepwise linear regression and principal component analysis) (Geladi and Kowalski, 1986; Kettaneh et al., 2005). The basic PLSR algorithm is not described in this paper but can be found elsewhere (Umetrics, 2012; Vinzi et al., 2010; Wold et al., 2001). We used the software of SIMCA-P + 13.0 (https://umetrics.com) to perform the PLSR. Using PLSR, the influence and importance of a predictor on the response variable was indicated by the variable importance for the projection (VIP) (Umetrics, 2012; Wold et al., 2001). Those terms with high VIP were the most relevant for explaining the dependent variable, and predictors with VIPs lower than 1.0 were considered of minor importance for prediction purposes (Umetrics, 2012; Wold et al., 2001). To overcome the problem of over-fitting, the appropriate number of components to be included in the PLSR model was determined by cross-validation to find an optimal balance between the explained variation in the determined coefficient (R^2) and the predictive ability of the model (goodness of prediction, Q^2) (Geladi and Kowalski, 1986; Wold et al., 2001). The root-mean-square error of cross validation (RMSECV) was used to evaluate the accuracy of the prediction. The optimal number of PLSR components often corresponds to a maximum Q^2 and a minimal RMSECV. The R^2, Q^2 and RMSECV were calculated as follows:

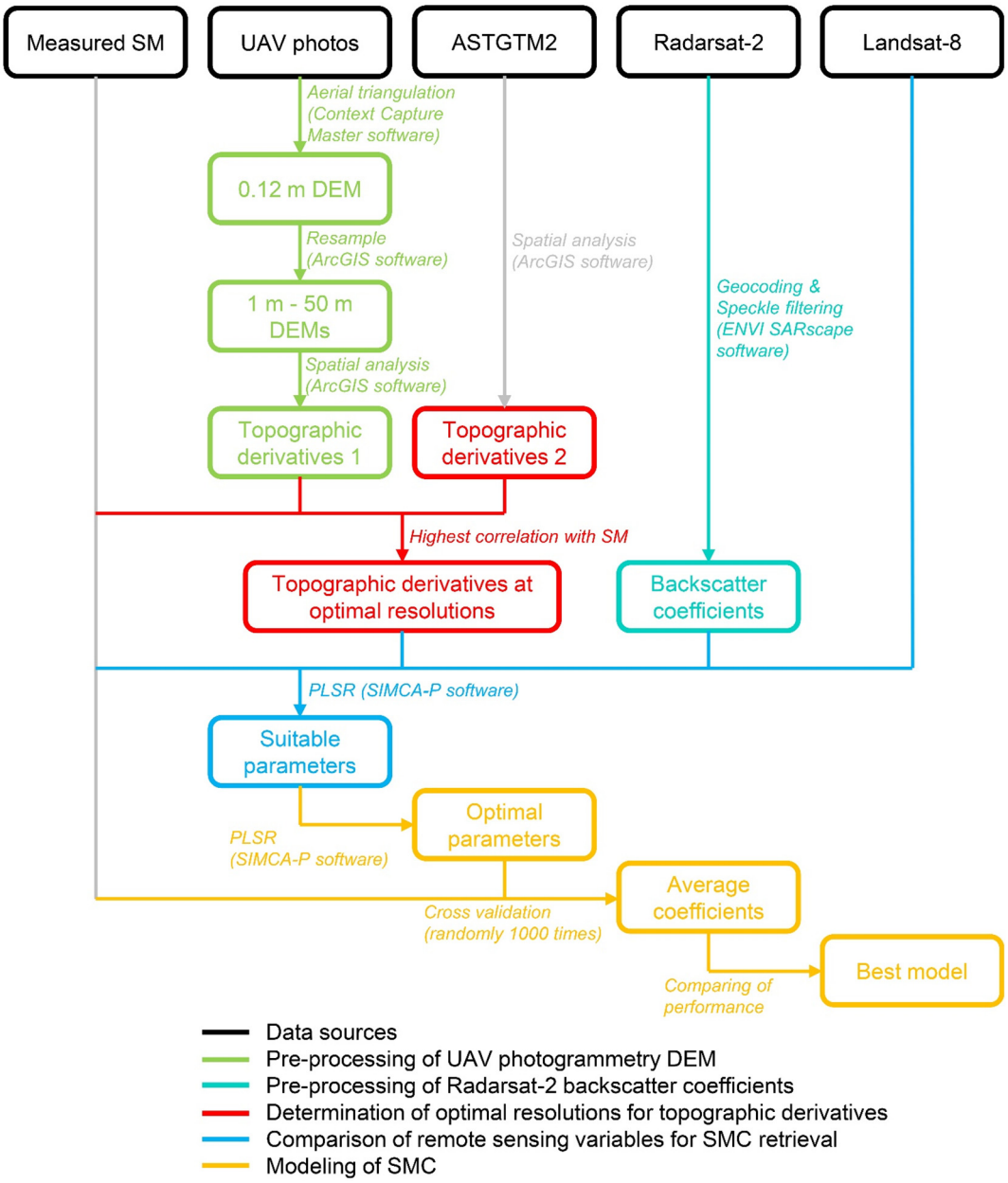

Fig. 2. Workflow. Certain part of the procedure is marked by certain color. (For interpretation of the references to color in this figure legend, the reader is referred to the web version of this article.)

$$R^2 = \frac{[\sum_{i=1}^{n}(P_i - P_m)(O_i - O_m)]^2}{\sum_{i=1}^{n}(P_i - P_m)^2(O_i - O_m)^2} \quad (1)$$

$$Q^2 = 1.0 - PRESS/SS \quad (2)$$

$$PRESS = \sum_{i=1}^{n}(\widehat{P}_i - O_i)^2 \quad (3)$$

$$SS = \sum_{i=1}^{n}(P_i - O_i)^2 \quad (4)$$

$$RMSECV = \sqrt{\frac{PRESS}{n}} \quad (5)$$

where P_i and O_i are the predicted and observed SM at each sampling point, n is the number of sampling points (n = 222), P_m and O_m are mean of the predicted and observed SM, *PRESS* is the prediction error sum of squares, *SS* is the residual sum of squares and $\widehat{P}_i$ is the predicted SM for the leave-one-out sample.

2.8. Modeling of soil moisture

Since there was a broad spectrum of variables (n = 30; Table 1) for spatial analyses and the number will often depend on statistical accuracy desired, there were too many variables determined to be of major importance. To simplify the modeling, another PLSR (variables with VIP being higher than 1.0 in Section 2.6 as the inputs) was done to reduce the number of predictors for SM modeling. Then, several linear models from complex to simple were built. Simple models had less predictors than complex models. Predictors with higher VIP were reserved for simple models while predictors with lower VIP were removed one by one. Having determined the optimal predictors for SM modeling, the entire data set (n = 222) was divided into calibration (75% of observations; n = 167) and validation (25% of observations; n = 55), and multiple linear regression was employed to quantify the relationship

Table 1
Abbreviations and descriptions of the potential predictors for SM estimation.

Predictors	Abbr.	Description
Landsat-8		
Band1 Coastal	B1	433–453 nm wavelengths.
Band 2 Blue	B2	450–515 nm wavelengths.
Band 3 Green	B3	525–600 nm wavelengths.
Band 4 Red	B4	630–680 nm wavelengths.
Band 5 Near-infrared	B5	845–885 nm wavelengths.
Band 6 SWIR 1	B6	1560–1660 nm wavelengths.
Band 7 SWIR 2	B7	2100–2300 nm wavelengths.
Band 8 Panchromatic	B8	500–680 nm wavelengths.
Band 9 Cirrus	B9	1360–1390 nm wavelengths.
Normalized difference vegetation index	NDVI	$NDVI = (B5 - B4)/(B5 + B4)$.
Radarsat-2		
VV polarization	VV	Backscatter coefficient of vertical-vertical polarization.
VH polarization	VH	Backscatter coefficient of vertical-horizontal polarization.
HV polarization	HV	Backscatter coefficient of horizontal-vertical polarization.
HH polarization	HH	Backscatter coefficient of horizontal-horizontal polarization.
Topographic derivatives		
Height index	HI	$HI = (H_{point} - H_{bottom})/(H_{peak} - H_{bottom})$, H_{point} is the elevation of the sampling point, H_{peak} and H_{bottom} are the elevation of the peak and bottom of the hillslope where the sampling point located.
Slope gradient	SLOPE	Rate of maximum change in elevation.
Aspect from north to south	ASPECT	$ASPECT = \cos(aspect * \pi/180)$, where *aspect* is expressed in positive degrees from 0 to 359.9, measured clockwise from north.
Surface curvature	SURF	The second derivative of the surface, or the slope of the slope. A positive curvature indicates the surface is upwardly convex at that cell.
Plan curvature	PLAN	The plan curvature is perpendicular to the direction of maximum slope. A positive value indicates the surface is upwardly convex at that cell.
Profile curvature	PROF	The profile curvature is in the direction of the maximum slope. A negative value indicates the surface is upwardly convex at that cell.
Flow accumulation	FACC	Flow accumulation is a raster of accumulated flow to each cell, as determined by accumulating the weight for all cells that flow into each downslope cell.
Topographic wetness index	TWI	$TWI = \ln(FACC/\tan SLOPE)$.

Notes: topographic derivatives calculated by ASTGTM2 DEM were marked by number "1" behind the abbreviations, such as HI1, SLOPE1, etc. Topographic derivatives calculated by UAV photogrammetry DEM were marked by number "2" behind the abbreviations, such as HI2, SLOPE2, etc.

between SM and the selected variables. Cross validation was completed by performing calibration and validation randomly 1000 times (based on the 222 samples, randomly select 1000 groups of data for calibration and validation). Then, mean regression coefficients of those 1000 models were used to generate the final model. Consequently, the final model was evaluated using 222 samples, based on Akaike's Information Criterion (AIC), the root mean square error (RMSE), and the coefficient determination (R^2). The following equations represent these statistical metrics:

$$AIC = \ln\left[\frac{1}{n}\sum_{i=1}^{n}(O_i - P_i)^2\right] + \frac{2h}{n} \quad (6)$$

$$RMSE = \sqrt{\frac{1}{n}\sum_{i=1}^{n}(O_i - P_i)^2} \quad (7)$$

$$R^2 = \frac{[\sum_{i=1}^{n}(P_i - P_m)(O_i - O_m)]^2}{\sum_{i=1}^{n}(P_i - P_m)^2(O_i - O_m)^2} \quad (8)$$

Table 2
Statistic of environmental factors.

Environmental factors	Units	Minimum	Maximum	Mean	Median	Standard deviation
Vegetation and bare rock						
Vegetation type	–	–	–	–	–	–
Bare rock coverage	m^2/m^2	0.00	0.85	0.21	0.20	0.17
Soil properties						
Soil moisture	cm^3/cm^3	0.15	0.57	0.35	0.35	0.09
Bulk density	$g/100\ cm^3$	40.3	145.11	99.47	100.67	20.61
Sand	g/100 g	5.56	63.45	23.30	20.53	11.53
Clay	g/100 g	1.73	34.12	12.90	11.87	6.33
Soil total nitrogen	g/kg	1.24	13.02	3.97	3.43	1.92
Soil total phosphorus	g/kg	0.16	1.60	0.57	0.56	0.19
Soil organic carbon	g/kg	15.95	192.91	47.45	36.87	26.99
Topographic derivatives						
Height index	–	0.00	0.96	0.32	0.28	0.30
Slope gradient	Degree	0.43	53.66	26.27	30.10	13.70
Aspect from north to south	–	−1.00	1.00	−0.13	−0.27	0.77
Surface curvature	–	−2.67	4.44	0.00	−0.18	1.20
Plan curvature	–	−2.29	2.57	0.19	0.06	0.73
Profile curvature	–	−1.52	2.66	0.26	0.28	0.64
Flow accumulation	m^2	0.00	1320.00	26.23	3.00	122.14
Topographic wetness index	–	0.00	19,397.79	419.94	5.35	2283.97

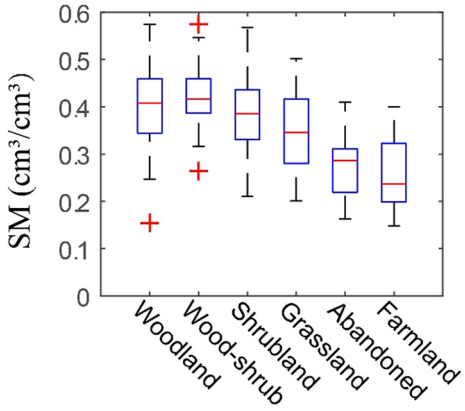

Fig. 3. Soil moisture distribution in different vegetation type.

where n is the number of the estimations, P_i and O_i are the predicted and observed SM ($cm^3\,cm^{-3}$) at each sampling point, respectively, P_m and O_m are the mean value of predicted and observed SM ($cm^3\,cm^{-3}$), respectively, and h is the number of estimated variables.

3. Results

3.1. Statistics of soil moisture and environmental factors

The SM of the 222 sampling points ranged from 0.15 to 0.57 $cm^3\,cm^{-3}$ (0.35 ± 0.09 $cm^3\,cm^{-3}$, mean ± standard deviation) (Table 2, Fig. 3). SM showed different distribution patterns in woodland, wood-shrubland, shrubland, grassland, abandoned land and farmland. The bare rock coverage of sampling points ranged from 0 to 85 $m^2\,m^{-2}$ (0.21 ± 0.17 $m^2\,m^{-2}$). The soil bulk density ranged from 40.3 to 145.11 $g\,cm^{-3}$ (99.47 ± 20.61 $g\,cm^{-3}$). The soil textures were mainly silt (Fig. 4). The soil total nitrogen ranged from 1.24 to 13.02 $g\,kg^{-1}$ (3.97 ± 1.92 $g\,kg^{-1}$). The soil total phosphorus ranged from 0.16 to 1.60 $g\,kg^{-1}$ (0.57 ± 0.19 $g\,kg^{-1}$). The soil organic carbon ranged from 15.95 to 192.91 $g\,kg^{-1}$ (47.45 ± 26.99 $g\,kg^{-1}$). The HI ranged from 0 to 0.96 (0.32 ± 0.30). The SLOPE ranged from 0 to 54° (26 ± 14°). Aspect ranged from −1 to 1 (−0.13 ± 0.77). Surface curvature ranged from −2.67 to 4.44 (0.00 ± 1.20). Plan curvature ranged from −2.29 to 2.57 (0.19 ± 0.73). Profile curvature ranged from −1.52 to 2.66 (0.26 ± 0.64). Flow accumulation ranged from 0 to 337,920 m^2 (6714 ± 31,268 m^2). Topographic wetness index ranged from 0.00 to 46,715 (1011 ± 5500). Details for these environmental factors are shown in Table 2.

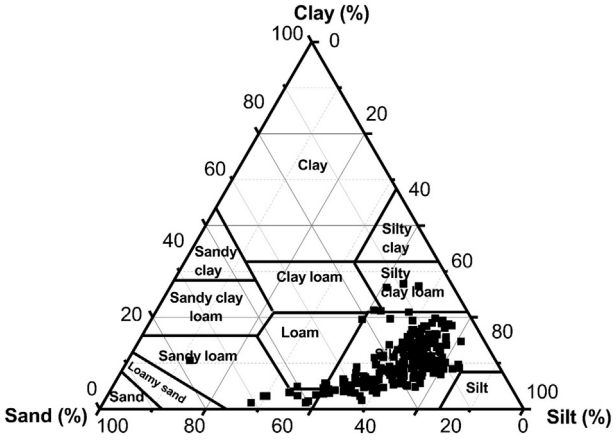

Fig. 4. Soil textures of 222 sampling points.

Table 3
Results of generalized linear model stepwise.

Environmental factors	Explained variability in SM (%)	Total explained variability (%)
Vegetation type	35.7	35.7
Aspect	7.7	43.4
Height index	4.2	47.6
Soil bulk density	3.3	50.9
Soil total nitrogen	3.1	54.0
Aspect * vegetation type	3.4	57.4
Soil total phosphorus	1.3	58.8

3.2. Major controlling factors of soil moisture

Results of generalized linear model stepwise showed that, vegetation type explained variability in SM of 35.7%, aspect explained variability in SM of 7.7%, height index explained variability in SM of 4.2%, bulk density explained variability in SM of 3.3%. Soil total nitrogen explained variability in SM of 3.1%. The interaction of aspect and vegetation type explained variability in SM of 3.3%. Soil total phosphorus explained variability in SM of 1.3%. The model totally explained variability in SM of 58.8%. Details for the generalized linear model stepwise are shown in Table 3.

3.3. Georeferencing precision of UAV photogrammetry

In Table 4 calculated the georeferencing precision of the UAV photogrammetry. Residual errors on ground control points were calculated for the DEM processed with the two workflows. For the DEM which was georeferenced by ground control points, the RMSE of the ground control points was 0.09 m in 3D. Moreover, for the DEM which was direct georeferenced by on-board GPS, the RMSE on ground control points was 1.46 m in 3D.

3.4. Optimal resolutions of topographic derivatives

The correlation coefficient between SM and ASTGTM2 derived topographic derivatives (R_{AST}) was lower than the correlation coefficient between SM and UAV-derived topographic derivatives (R_{UAV}) most of time. For HI (Fig. 5.a), the R_{UAV} were stable from 1 m to 50 m resolutions. For SLOPE and ASPECT (Fig. 5.b, c), the R_{UAV} reached their

Table 4
Georeferencing precision of UAV photogrammetry.

Georeferencing methods and control points	3D horizontal error (m)	3D vertical error (m)	3D error (m)	3D RMSE (m)
Ground control points georeferencing				0.09
Control point 1	0.07	−0.18	0.19	
Control point 2	0.03	0.08	0.08	
Control point 3	0.10	−0.03	0.10	
Control point 4	0.04	−0.02	0.04	
Control point 5	0.02	−0.01	0.02	
Control point 6	0.00	0.00	0.00	
Control point 7	0.08	0.06	0.10	
Control point 8	0.00	0.00	0.00	
On-board GPS direct georeferencing				1.46
Control point 1	0.69	1.13	1.33	
Control point 2	0.67	1.39	1.54	
Control point 3	0.65	1.28	1.44	
Control point 4	0.65	1.29	1.44	
Control point 5	0.66	1.30	1.46	
Control point 6	0.67	1.31	1.47	
Control point 7	0.65	1.37	1.52	
Control point 8	0.67	1.31	1.47	

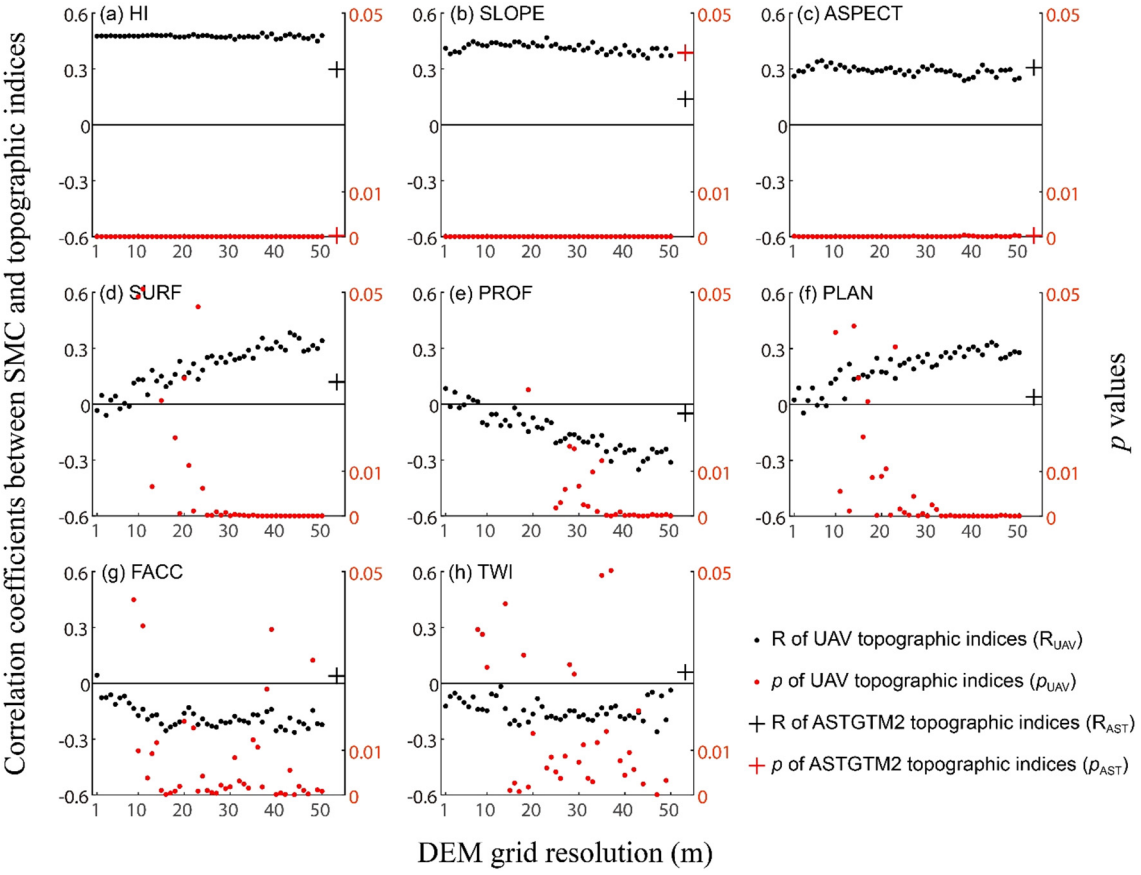

Fig. 5. Pearson correlation coefficients between SM and topographic derivatives. Correlation coefficients between SM and UAV-derived topographic derivatives from 1 m to 50 m resolutions were scattered by black points which belong to left Y axis, with the matching *p* values scattered by red points which belong to right Y axis. Besides, at the last column, the correlation coefficients and *p* values between SM and ASTGTM2-derived topographic derivatives of 30 m resolution were marked by black and red cross. *p* values > 0.05 were not marked. The abbreviations for the variables are listed in Table 1. (For interpretation of the references to color in this figure legend, the reader is referred to the web version of this article.)

highest value at 7 m resolution. For SURF, PROF and PLAN (Fig. 5.d, e, f), significant correlations ($p_{UAV} < 0.05$) were shown after the 20 m resolution, and the R_{UAV} reached the highest value at a resolution of 43 m. For FACC and TWI (Fig. 5.g, h), significant correlations ($p_{UAV} < 0.05$) were shown after the 13 m resolution, and the R_{UAV} reached the highest value at a resolution of 16 m, and R_{UAV} and p_{UAV} (significance) showed no clear pattern after 30 m resolution. In terms of maximum R values, the optimal resolutions were 7 m for HI, SLOPE and ASPECT, 43 m for SURF, PROF and PLAN, 16 m for FACC and TWI.

3.5. Importance of remote sensing variables for SM estimation

Fig. 6 illustrates the VIP and the scaled regression coefficient for each variable in the PLSR (mentioned in Section 2.6). Note that all the considered variables might be related to the SM to some extent, however, only certain variables had VIP higher than 1.0. The highest VIPs were obtained for B3 (1.51) and B5 (1.50), followed by HI2 (1.45), B1 (1.42), B8 (1.42), NDVI (1.37), B2 (1.37), SLOPE2 (1.33), B6 (1.30), B7 (1.26), B4 (1.26), SURF2 (1.07) and PROF2 (1.03). Higher HI2, SLOPE2, SURF2, and B4 corresponded with higher SM (as indicated by the positive regression coefficients), while the opposite was found for

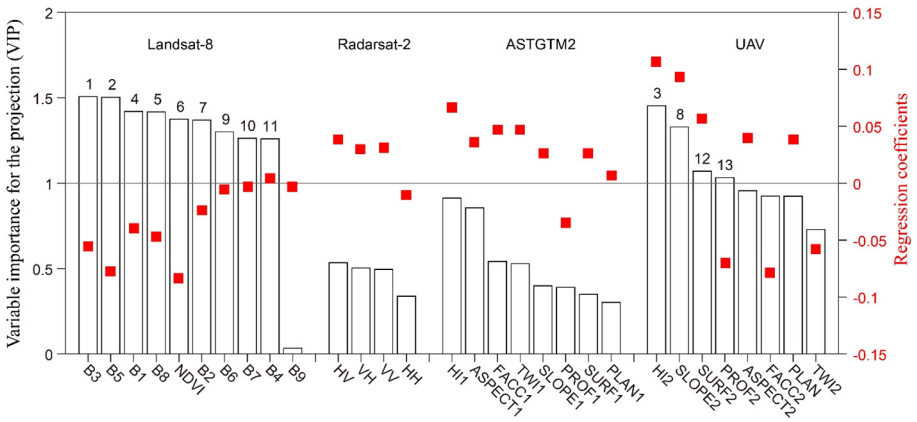

Fig. 6. Variable importance for the projection (bar) and regression coefficients (dot) of each predictor in PLSR. The predictors were ranked within each group (Landsat-8, Radarsat-2, ASTGTM2, UAV) in descending order based on their VIP. The important predictors with VIP being higher than 1.0 are consecutively numbered to show their relative importance. Scaled regression coefficients show the direction in which the predicted response (SM) depends on the predictors. The straight solid line (VIP = 1.0) indicates a threshold above which the predictors are considered to be important for predictive purposes. The abbreviations for the variables are listed in Table 1. Topographic derivatives derived from ASTGTM2 and UAV are distinguished by 1 and 2, respectively.

Table 5
Predictive performance of linear regression models.

Models	Calibration (n = 167)		Validation-A (n = 55)	Validation-B (n = 222)		
	$\overline{RMSE}$	$\overline{R^2}$	$\overline{RMSE}$	$\overline{R^2}$	*AIC*	*RMSE*	R^2
$M1: SM = 8.50 * 10^{-2}HI - 1.51 * 10^{-5}B5 + 1.66 * 10^{-4}B3 - 9.89 * 10^{-5}B8 - 1.67 * 10^{-4}B1 - 0.132NDVI + 7.77 * 10^{-4}SLOPE + 1.49$	0.074	0.39	0.074	0.35	−2.186	0.074	0.38
$M2: SM = 9.61 * 10^{-2}HI - 6.17 * 10^{-6}B5 + 1.11 * 10^{-4}B3 - 9.19 * 10^{-5}B8 - 1.12 * 10^{-4}B1 - 0.318NDVI + 1.32$	0.074	0.38	0.074	0.35	−2.191	0.075	0.38
$M3: SM = 9.59 * 10^{-2}HI - 2.20 * 10^{-5}B5 + 1.40 * 10^{-4}B3 - 8.41 * 10^{-5}B8 - 1.21 * 10^{-4}B1 + 1.23$	0.074	0.38	0.074	0.35	−2.199	0.075	0.38
$M4: SM = 9.52 * 10^{-2}HI - 1.91 * 10^{-5}B5 + 9.07 * 10^{-5}B3 - 8.89 * 10^{-5}B8 + 0.499$	0.074	0.38	0.074	0.35	−2.207	0.075	0.38
$M5: SM = 8.68 * 10^{-2}HI - 1.23 * 10^{-5}B5 - 3.86 * 10^{-5}B3 + 0.760$	0.075	0.37	0.075	0.35	−2.208	0.075	0.36
$M6: SM = 9.27 * 10^{-2}HI - 1.82 * 10^{-5}B5 + 0.519$	0.075	0.36	0.075	0.36	−2.214	0.076	0.36

Notes: For building the models, the entire data set was divided into calibration (75% of observations; n = 167) and validation (Validation-A; 25% of observations; n = 55). Cross validation was used to avoid contingency, and 1000 times of calibration and validation were processed randomly. Then, mean coefficients of these 1000 models formed an average model (M1–M6). Finally, a new validation (Validation-B; 100% of observations; n = 222) for each average model was made. *AIC*, Akaike's information criterion; *RMSE*, root mean square error; R^2, determination coefficient; *RMSE*, mean *RMSE* of the 1000 times of validation; R^2, mean R^2 of the 1000 times of validation.

Fig. 7. Plots of the observed and predicted SM. This plot displays the observed versus predicted values of the 222 sampling points of the strongest model ($SM = 9.27 * 10^{-2}HI - 1.82 * 10^{-5}B5 + 0.519$). Height index (HI) is a precise description of sampling points' location on hillslope, detailed in Table 1. B5 is the near-infrared band of Landsat-8, detailed in Table 1. R^2 is fraction of SM-variation modeled which indicates the goodness of fit. RMSE is the root mean square error of the fit for observations in the model.

PROF2, NDVI, B1, B2, B3, B5, B6, B7 and B8 (as indicated by the negative regression coefficients).

The VIPs for UAV based variables were often significantly higher than those from the ASTGTM2 (Fig. 6). There were increasing differences between these two groups in the following order: HI (0.91 vs. 1.45, ASTGTM2 vs. UAV), SLOPE (0.39 vs. 1.33), SURF (0.35 vs. 1.07), PROF (0.39 vs. 1.03), PLAN (0.30 vs. 0.92), FACC (0.54 vs. 0.92), ASPECT (0.86 vs. 0.96), TWI (0.53 vs. 0.73).

3.6. Variables selection and the performance of the SM estimation

As mentioned in Section 3.3 above, seven variables with VIP higher than 1.0 were selected using this method for SM estimation (Table 5). Table 5 shows the performance of 6 regression models with different predictors. For Validation-B (n = 222), with the decreasing number of predictors, the AIC decreased from −2.186 to −2.214, RMSE increased from 0.074 to 0.076, and R^2 decreased from 0.38 to 0.36. The AIC was the lowest value in model 'M6'. The scatter plot (Fig. 7) shows the Validation-B (n = 222) of 'M6'.

4. Discussion

Based on the Landsat-8, Radarsat-2, ASTGTM2, and UAV photogrammetry DEM, and 222 soil sampling observations, this study investigated the major controlling factors of soil moisture and assessed the relative importance of different variables (optical and infrared bands, microwave backscatter coefficients, topographic derivatives) in SM estimation in a karst mountainous catchment.

4.1. Major controlling factors of SM

According to the generalized linear stepwise, vegetation type, aspect, height index, soil bulk density, soil total nitrogen and soil total phosphorus showed good explanation to SM (Table 3), which indicated that vegetation cover, topography and soil properties were the major controlling factors to SM in karst region. After a dry winter, SM had

higher value in wood-shrub land, woodland and shrubland, and had lowest value in farmland (Fig. 3), which indicated wood and shrub might have a greater tolerance to extreme drought under climate change (Tong et al., 2018).

4.2. Predictors selection for SM remote sensing

According to the PLSR analysis, the optical (B1, B2, B3, B4) and infrared bands (B5, B6, B7) and part of topographic derivatives (HI, SLOPE, SURF, PROF) exhibited high VIP (Fig. 4), which indicated that these variables were more sensitive to SM than those with lower VIP and had potential to be the predictors for SM remote sensing. The optical and infrared bands can estimate SM by observing vegetation growth conditions as vegetation cover has some linkage to SM (Chen et al., 1996; Raich and Tufekcioglu, 2000). As for the topographic derivatives, they determine the lateral transport of runoff, SM accumulation, and solar radiation, which are strongly related to distribution of SM (Beldring et al., 1999; Burt and Butcher, 1985). Therefore, results of the analysis on SM major controlling factors were consistent with the results of predictors selection for SM remote sensing, which provided the basis for the following modeling of SM remote sensing.

The NDVI had relatively high VIP (1.37), which indicated that vegetation is an important predictor for SM. However, negative correlations between NDVI and SM were found in this study. This might be attributed to the timing of the field sampling, which occurred in March, as it was the start of the growing season for crops. Crops had lush foliage which led to high NDVI values but also high water consumption by plants (and therefore low SM). As for shrubs and woods, it was still the dormant period for the vegetation in March which led to low NDVI values and low water consumption by vegetation (and therefore high SM). Similar results have been found in previous studies (Daubenmire, 1968; Ma et al., 2004; Méndez-Barroso et al., 2009; Unger and Kaspar, 1994).

In contrast to the variables from Landsat-8, the Radarsat-2 variables showed no significant correlations to SM (the highest VIP was 0.71) (Fig. 4), which indicated that the variables represented by microwaves might be of minor importance for SM estimation in this region. However, previous studies demonstrated a strong relationship between backscatter and moisture in the bare fields (Dubois et al., 1995; Fung et al., 1992; Oh et al., 1992). This can be attributed to high scatter of the microwaves in heterogeneous mountainous regions, which results in severe interference of the backscatter (Lakhankar et al., 2009; Li et al., 2014b; Mätzler and Standley, 2000). Ancillary information (vegetation water content (Ceccato et al., 2001), canopy structure (Clark et al., 2004), soil surface roughness (Jester and Klik, 2005) and dead vegetation (Xu et al., 2014)) is needed in natural landscapes to use microwaves to assess SM (Wigneron et al., 2003). However, this ancillary information is difficult to gather, especially in variable terrain and landscapes (Kornelsen and Coulibaly, 2013). Thus, it is still a challenge to use microwave remote sensing for SM in heterogeneous mountainous areas.

4.3. Optimal resolutions for topographic derivatives

The highly heterogeneous landscape resulted in topography influencing SM. The results showed that the correlation between topographic derivatives and SM varied with DEM grid resolution (Fig. 3). The finest resolution did not show the strongest correlations to SM (Fig. 3). This may be because the microtopography does not dominate the hydrological processes of the landscape (Sørensen and Seibert, 2007; Thomas et al., 2017). Generally, the correlation initially increased with an increase in the DEM resolution to its highest value at the optimal resolution, and then decreased (Fig. 3). This result suggested that optimal resolution may represent a balance of hydrological effects from microtopography (small scale) and the hillslope (relative larger scale) (Cavazzi et al., 2013; Smith et al., 2006; Thomas et al., 2017). The variation of resolution had no significant influence on height index and aspect, the reason should be that the long slope length made the height index and aspect calculated in different DEMs (1–50 m) almost the same. The optimal resolution of slope gradient was 7 m, which indicated that the corresponding unit of surface runoff (Thomas et al., 2017) mainly ranged within meters in this region. The optimal resolution of curvatures was 43 m, the reason should be that the curvatures calculated in such resolution correlated well with height index (sampling points with positive value of curvatures located at the mountain top which had high height index). Curvatures, flow accumulation and topographic wetness index calculated in meters resolution had no correlation with SM, which indicated that surface relief in meters scale had no significant effect on SM distribution.

4.4. Potential of UAV photogrammetry on hydrological research

Comparing UAV DEM with ASTGTM2 at the same resolution (30 m), topographic derivatives obtained from the UAV photogrammetry DEM had higher correlations with SM than those from ASTGTM2 (Fig. 3). The reason might be that the UAV aerial triangulation has higher precision (RMSE = 0.09 m) (Gindraux et al., 2017; Gonçalves and Henriques, 2015), and the lower precision of ASTGTM2 results in errors on steep hillslopes, especially in mountainous areas (DeWitt et al., 2015; Hirano et al., 2003; Holmesa et al., 2000; Mukherjee et al., 2013). Results of the PLSR showed that HI, SLOPE, SURF and PROF were strongly correlated with SM (Fig. 4). However, FACC and TWI exhibited low VIP (Fig. 4), and the reason may be that the FACC does not consider evaporation and percolation. In karst region in southwest China, the large number of cracks and conduits in the carbonate bed rock can result in water leakage through these conduits (Li et al., 2017; Zhang et al., 2014) and therefore the flow accumulation area derived from DEM might not represent the real flow accumulation of the sample site.

With respect to the choice of DEM data sources, there are three primary options: interferometric synthetic aperture radar, photogrammetry, and LIDAR. They are suitable for different fields according to the platform (DeWitt et al., 2015). Space borne DEMs are suitable for regional research as they have the advantage of capturing images over a large spatial area; aerial borne DEMs are suitable for catchment hydrological research due to their high resolution and high precision; and LIDAR is known as the most reliable method since it has the highest precision. However, UAV photogrammetry has a competitive advantage over LIDAR in terms of usability and cost (Colomina and Molina, 2014). Wilkinson et al. (2016) confirmed that both LIDAR and photogrammetry methods are suitable for the acquisition of outcrop. Previous studies applied UAV photogrammetry on research of soil erosion, and the quality was encouraging (D'Oleire-Oltmanns et al., 2012; Pineux et al., 2017). Compared to ASTGTM2 topographic derivatives, this study shows a higher correlation of UAV topographic derivatives with SM (Fig. 3) and a much higher VIP in PLSR analysis (Fig. 5). Moreover, the precision of the UAV photogrammetry DEM in this study (RMSE = 0.09 m) was precise enough for the calculation of topographic derivatives on their optimal resolution (7 m). Even more, the simplest direct georeferenced triangulation was qualified to these calculations to some extent, since its horizontal error was < 0.7 m and the relative height difference (vertical error) did not affect the calculation (Table 4). Thus, while high-resolution and high-precision elevation data are temporally limited, UAV photogrammetry is a good choice for catchment hydrological research.

4.5. Soil moisture remote sensing model

According to the VIP, 7 predictors were selected to develop multiple linear regression model for SM estimation (Table 3). The model (M6) took HI and B5 as predictors, which suggested that topography and vegetation are important factors for soil moisture estimation. Previous studies also illustrated the importance of topography and vegetation on

soil moisture remote sensing. For example, Vivoni et al. (2008a) found no significant correlation between SM and radar signal in a region with high topographic and vegetation variability (northern Sonora, Mexico), and pointed out that hypsometric averaging ($R^2 = 0.57$) could improve the basin average SM estimation compared to arithmetic averaging ($R^2 = 0.09$), and suggested that topographic information could improve SM estimation. Méndez-Barroso et al. (2009) analyzed vegetation dynamics using remotely-sensed enhanced vegetation index images, results indicated that changes in vegetation greenness were directly related to hydrologic conditions and also correlated well with soil moisture. Peng and Wang (2012) analyzed sixty-one rainfall events at the same catchment as ours, results demonstrated that surface runoff was affected by vegetation cover. Inevitably, SM was affected by vegetation cover. Liu et al. (2016) confirmed that portion of karst landform and vegetation cover were the most influencing factors for actual evapotranspiration in this region, which in turn affected the hydrologic processes. From the above, lots of studies drew similar conclusions on the importance of topography and vegetation, which provided good supports for our validity and conclusions.

The soil moisture estimation model (M6) had the determination coefficient of 0.36 (Fig. 5) at point scale. Since few studies accessed the evaluation of SM remote sensing models on point scale in karst catchments, we can only evaluate the reliability of our model based on comparing our accuracy with globally averaged accuracy. Dorigo et al. (2015) evaluated the ESA CCI (European Space Agency's Water Cycle Multi-Mission Observation Strategy and Climate Change Initiative projects) soil moisture product using ISMN (the International Soil Moisture Network) ground-based observations, and the average R^2 between remote sensed soil moisture and in-situ observations was 0.21. Colliander et al. (2017) validated the SMAP (NASA Soil Moisture Active Passive mission) surface soil moisture products with 13 validation sites over the 2.5-month period in 2015, and the average R^2 of all sites was 0.22. Wagner et al. (2003) evaluated the agreement between ERS (European Remote Sensing Satellites) surface soil moisture product with model and precipitation data, results showed that mountain area SM estimation had the worst accuracy and ranked last 5% globally. Compared to these studies, our study was conducted in the most challenging area (the complex structure of earth's critical zone led to complex SM variation), but the performance of M6 ($R^2 = 0.36$) was still better than global average level ($R^2 = 0.22$). Thus, the performance of M6 might be acceptable.

Overall, the topographic and vegetation information were important for improving SM estimation (Fig. 4). As for the topographic derivatives, the resolution affected their sensitivity to SM (Figs. 3, 4). The final model, based on the selected predictors with relatively high VIP, exhibited acceptable accuracy. These results provide helpful suggestions for SM estimation in heterogeneous mountainous catchments. Further study is needed to fully understand the mechanism of microwave scattering in these landscapes.

5. Conclusions

Based on the Landsat-8, Radarsat-2, ASTGTM2, UAV photogrammetry DEM, and 222 soil sampling observations, this study investigated the major controlling factors of SM and made an attempt on SM remote sensing in karst mountainous catchments. Results showed that vegetation type (35.7%), aspect (7.7%), height index (4.2%), soil bulk density (3.3%), soil total nitrogen (3.1%), aspect interact with vegetation type (3.4%) and soil total phosphorous (1.3%) totally explained 58.8% of the SM variability. Among all the vegetation types, wood-shrubland, woodland and shrubland had relatively higher SM, while abandoned land and farm land had relatively lower SM, which indicated wood and shrub might have a greater tolerance to extreme drought under climate change. The correlation between topographic derivatives and SM varied with the DEM resolution. The optimal resolution was 7 m for height index, slope gradient and aspect from north to south, 43 m for surface curvature and profile curvature and plan curvature, 16 m for flow accumulation and topographic wetness index. The UAV photogrammetry DEM had good precisions both for ground control points georeferencing (RMSE = 0.09 m) and on-board GPS direct georeferencing (RMSE = 1.46 m), which were precise enough to calculate topographic derivatives on their optimal resolutions. Meanwhile, compared to the ASTGTM2, the UAV-derived topographic derivatives showed higher correlations to SM, suggesting that UAV photogrammetry has potential use in catchment hydrological research. According to the PLSR results, the optimal predictors with high VIP, including HI, SLOPE, B1, B3, B5, B8 and NDVI, were selected out to develop the SM estimation model. The relatively high determination coefficient ($R^2 = 0.36$) indicated that the accuracy of final model ($SM = 9.27E^{-2}HI - 1.82E^{-5}B5 + 0.519$) was acceptable. Though the R^2 of the final model was still low, these results provide useful information for soil moisture remote sensing in karst mountainous areas and similar heterogeneous landscapes.

Acknowledgements

This study was financially supported by the National Natural Science Foundation of China, China (Nos. 41501478, 41571130073 and 41471233), and Youth Innovation Team Project of Institute of Subtropical Agriculture, Chinese Academy of Sciences, China (2017QNCXTD_XXL). This work was conducted in Chenqi and Dengzhanhe catchments, which are supported and managed by the Puding Karst Ecosystem Research Station. Assistance in the field data collections and maintenance from the Puding Karst Ecosystem Research Station is gratefully acknowledged.

References

Appels, W.M., Bogaart, P.W., van der Zee, S.E.A.T.M., 2011. Influence of spatial variations of microtopography and infiltration on surface runoff and field scale hydrological connectivity. Adv. Water Resour. 34, 303–313.
Ariza-Villaverde, A.B., Jiménez-Hornero, F.J., Gutiérrez De Ravé, E., 2015. Influence of DEM resolution on drainage network extraction: a multifractal analysis. Geomorphology 241, 243–254.
Baldwin, D., Naithani, K.J., Lin, H., 2017. Combined soil-terrain stratification for characterizing catchment-scale soil moisture variation. Geoderma 285, 260–269.
Beldring, S., Gottschalk, L., Seibert, J., Tallaksen, L.M., 1999. Distribution of soil moisture and groundwater levels at patch and catchment scales. Agric. For. Meteorol. 98–9, 305–324.
Bendel, R.B., Afifi, A.A., 1977. Comparison of stopping rules in forward "stepwise" regression. J. Am. Stat. Assoc. 72, 46–53.
Burt, T.P., Butcher, D.P., 1985. Topographic controls of soil-moisture distributions. J. Soil Sci. 36, 469–486.
Carlson, T., 2007. An overview of the "triangle method" for estimating surface evapotranspiration and soil moisture from satellite imagery. Sensors 7, 1612–1629.
Cavazzi, S., Corstanje, R., Mayr, T., Hannam, J., Fealy, R., 2013. Are fine resolution digital elevation models always the best choice in digital soil mapping? Geoderma 195-196, 111–121.
Ceccato, P., Flasse, S., Tarantola, S., Jacquemoud, S., Grégoire, J.-M., 2001. Detecting vegetation leaf water content using reflectance in the optical domain. Remote Sens. Environ. 77, 22–33.
Chang, C.W., Laird, D.A., Mausbach, M.J., Hurburgh, C.R., 2001. Near-infrared reflectance spectroscopy-principal components regression analyses of soil properties. Soil Sci. Soc. Am. J. 65, 480–490.
Chen, F., Mitchell, K., Schaake, J., Xue, Y., Pan, H.-L., Koren, V., Duan, Q.Y., Ek, M., Betts, A., 1996. Modeling of land surface evaporation by four schemes and comparison with FIFE observations. J. Geophys. Res. - Atmos. 101, 7251–7268.
Chen, X., Zhang, Z.C., Chen, X.H., Shi, P., 2009. The impact of land use and land cover changes on soil moisture and hydraulic conductivity along the karst hillslopes of southwest China. Environ. Earth Sci. 59, 811–820.
Chen, H., Zhang, W., Wang, K., Fu, W., 2010. Soil moisture dynamics under different land uses on karst hillslope in northwest Guangxi, China. Environ. Earth Sci. 61, 1105–1111.
Clark, M.L., Clark, D.B., Roberts, D.A., 2004. Small-footprint lidar estimation of sub-canopy elevation and tree height in a tropical rain forest landscape. Remote Sens. Environ. 91, 68–89.
Colliander, A., Jackson, T.J., Bindlish, R., Chan, S., Das, N., Kim, S.B., Cosh, M.H., Dunbar, R.S., Dang, L., Pashaian, L., Asanuma, J., Aida, K., Berg, A., Rowlandson, T., Bosch, D., Caldwell, T., Caylor, K., Goodrich, D., al Jassar, H., Lopez-Baeza, E., Martínez-Fernández, J., González-Zamora, A., Livingston, S., McNairn, H., Pacheco, A., Moghaddam, M., Montzka, C., Notarnicola, C., Niedrist, G., Pellarin, T., Prueger, J., Pulliainen, J., Rautiainen, K., Ramos, J., Seyfried, M., Starks, P., Su, Z., Zeng, Y.,

van der Velde, R., Thibeault, M., Dorigo, W., Vreugdenhil, M., Walker, J.P., Wu, X., Monerris, A., O'Neill, P.E., Entekhabi, D., Njoku, E.G., Yueh, S., 2017. Validation of SMAP surface soil moisture products with core validation sites. Remote Sens. Environ. 191, 215–231.
Colomina, I., Molina, P., 2014. Unmanned aerial systems for photogrammetry and remote sensing: a review. ISPRS J. Photogramm. Remote Sens. 92, 79–97.
Daubenmire, R., 1968. Soil moisture in relation to vegetation distribution in mountains of northern Idaho. Ecology 49, 431–438.
DeWitt, J.D., Warner, T.A., Conley, J.F., 2015. Comparison of DEMS derived from USGS DLG, SRTM, a statewide photogrammetry program, ASTER GDEM and LiDAR: implications for change detection. GIScience Remote Sens. 52, 179–197.
d'Oleire-Oltmanns, S., Marzolff, I., Peter, K., Ries, J., 2012. Unmanned aerial vehicle (UAV) for monitoring soil erosion in Morocco. Remote Sens. 4, 3390–3416.
Dorigo, W.A., Gruber, A., De Jeu, R.A.M., Wagner, W., Stacke, T., Loew, A., Albergel, C., Brocca, L., Chung, D., Parinussa, R.M., Kidd, R., 2015. Evaluation of the ESA CCI soil moisture product using ground-based observations. Remote Sens. Environ. 162, 380–395.
Dubois, P.C., Vanzyl, J., Engman, T., 1995. Measuring soil-moisture with imaging radars. IEEE Trans. Geosci. Remote Sens. 33, 915–926.
Fan, L., Xiao, Q., Wen, J., Liu, Q., Jin, R., You, D., Li, X., 2015. Mapping high-resolution soil moisture over heterogeneous cropland using multi-resource remote sensing and ground observations. Remote Sens. 7, 13273–13297.
Feng, H., Liu, Y., Wu, G., 2015. Temporal variability of uncertainty in pixel-wise soil moisture: implications for satellite validation. Remote Sens. 7, 5398–5415.
Fung, A.K., Li, Z.Q., Chen, K.S., 1992. Backscattering from a randomly rough dielectric surface. IEEE Trans. Geosci. Remote Sens. 30, 356–369.
Geladi, P., Kowalski, B.R., 1986. Partial least-squares regression: a tutorial. Anal. Chim. Acta 185, 1–17.
Gindraux, S., Boesch, R., Farinotti, D., 2017. Accuracy assessment of digital surface models from unmanned aerial vehicles' imagery on glaciers. Remote Sens. 9, 186.
Gonçalves, J.A., Henriques, R., 2015. UAV photogrammetry for topographic monitoring of coastal areas. ISPRS J. Photogramm. Remote Sens. 104, 101–111.
Hartmann, A., Goldscheider, N., Wagener, T., Lange, J., Weiler, M., 2014. Karst water resources in a changing world: review of hydrological modeling approaches. Rev. Geophys. 52, 218–242.
Harwin, S., Lucieer, A., 2012. Assessing the accuracy of georeferenced point clouds produced via multi-view stereopsis from unmanned aerial vehicle (UAV) imagery. Remote Sens. 4, 1573–1599.
Hirano, A., Welch, R., Lang, H., 2003. Mapping from ASTER stereo image data: DEM validation and accuracy assessment. ISPRS J. Photogramm. Remote Sens. 57, 356–370.
Holmesa, K.W., Chadwick, O.A., Kyriakidis, P.C., 2000. Error in a USGS 30-meter digital elevation model and its impact on terrain modeling. J. Hydrol. 223, 154–173.
Houser, P.R., Shuttleworth, W.J., Famiglietti, J.S., Gupta, H.V., Syed, K.H., Goodrich, D.C., 1998. Integration of soil moisture remote sensing and hydrologic modeling using data assimilation. Water Resour. Res. 34, 3405–3420.
ISO, 1998. ISO 11272: Soil Quality—Determination of Dry Bulk Density. International Organiztion for Standardization, Geneva, Switzerland.
Jackson, T.J., Schmugge, J., Engman, E.T., 2009. Remote sensing applications to hydrology: soil moisture. Hydrol. Sci. J. 41, 517–530.
Jester, W., Klik, A., 2005. Soil surface roughness measurement—methods, applicability, and surface representation. Catena 64, 174–192.
Jung, M., Reichstein, M., Ciais, P., Seneviratne, S.I., Sheffield, J., Goulden, M.L., Bonan, G., Cescatti, A., Chen, J., de Jeu, R., Dolman, A.J., Eugster, W., Gerten, D., Gianelle, D., Gobron, N., Heinke, J., Kimball, J., Law, B.E., Montagnani, L., Mu, Q., Mueller, B., Oleson, K., Papale, D., Richardson, A.D., Roupsard, O., Running, S., Tomelleri, E., Viovy, N., Weber, U., Williams, C., Wood, E., Zaehle, S., Zhang, K., 2010. Recent decline in the global land evapotranspiration trend due to limited moisture supply. Nature 467, 951–954.
Kettaneh, N., Berglund, A., Wold, S., 2005. PCA and PLS with very large data sets. Comput. Stat. Data Anal. 48, 69–85.
Kornelsen, K.C., Coulibaly, P., 2013. Advances in soil moisture retrieval from synthetic aperture radar and hydrological applications. J. Hydrol. 476, 460–489.
Kustas, W.P., Norman, J.M., 2009. Use of remote sensing for evapotranspiration monitoring over land surfaces. Hydrol. Sci. J. 41, 495–516.
Lakhankar, T., Ghedira, H., Temimi, M., Azar, A.E., Khanbilvardi, R., 2009. Effect of land cover heterogeneity on soil moisture retrieval using active microwave remote sensing data. Remote Sens. 1, 80–91.
Li, S., Ren, H.D., Xue, L., Chang, J., Yao, X.H., 2014a. Influence of bare rocks on surrounding soil moisture in the karst rocky desertification regions under drought conditions. Catena 116, 157–162.
Li, X., Zhang, L., Weihermuller, L., Jiang, L., Vereecken, H., 2014b. Measurement and simulation of topographic effects on passive microwave remote sensing over mountain areas: a case study from the Tibetan Plateau. IEEE Trans. Geosci. Remote Sens. 52, 1489–1501.
Li, Z., Xu, X., Xu, C., Liu, M., Wang, K., Yu, B., 2017. Annual runoff is highly linked to precipitation extremes in karst catchments of Southwest China. J. Hydrometeorol. 18, 2745–2759.
Liu, M., Xu, X., Sun, A.Y., Wang, K., Liu, W., Zhang, X., 2014. Is southwestern China experiencing more frequent precipitation extremes? Environ. Res. Lett. 9.
Liu, M., Xu, X., Wang, D., Sun, A.Y., Wang, K., 2016. Karst catchments exhibited higher degradation stress from climate change than the non-karst catchments in southwest China: an ecohydrological perspective. J. Hydrol. 535, 173–180.
Liu, M., Xu, X., Xu, C., Sun, A.Y., Wang, K., Scanlon, B.R., Zhang, L., 2017. A new drought index that considers the joint effects of climate and land surface change. Water Resour. Res. 53, 3262–3278.
Ma, K.M., Fu, B.J., Liu, S.L., Guan, W.B., Liu, G.H., Lu, Y.H., Anand, M., 2004. Multiple-scale soil moisture distribution and its implications for ecosystem restoration in an Arid River valley, China. Land Degrad. Dev. 15, 75–85.
Mätzler, C., Standley, A., 2000. Technical note: relief effects for passive microwave remote sensing. Int. J. Remote Sens. 21, 2403–2412.
Méndez-Barroso, L.A., Vivoni, E.R., Watts, C.J., Rodríguez, J.C., 2009. Seasonal and interannual relations between precipitation, surface soil moisture and vegetation dynamics in the North American monsoon region. J. Hydrol. 377, 59–70.
Moore, I.D., Grayson, R.B., Ladson, A.R., 1991. Digital terrain modelling: a review of hydrological, geomorphological, and biological applications. Hydrol. Process. 5, 3–30.
Mukherjee, S., Joshi, P.K., Mukherjee, S., Ghosh, A., Garg, R.D., Mukhopadhyay, A., 2013. Evaluation of vertical accuracy of open source Digital Elevation Model (DEM). Int. J. Appl. Earth Obs. Geoinf. 21, 205–217.
Napieralski, J., Nalepa, N., 2010. The application of control charts to determine the effect of grid cell size on landform morphometry. Comput. Geosci. 36, 222–230.
Nelder, J.A., Wedderburn, R.W.M., 1972. Generalized linear models. J. R. Stat. Soc. Ser. A (Gen.) 135, 370–384.
Niethammer, U., James, M.R., Rothmund, S., Travelletti, J., Joswig, M., 2012. UAV-based remote sensing of the Super-Sauze landslide: evaluation and results. Eng. Geol. 128, 2–11.
Oh, Y., Sarabandi, K., Ulaby, F.T., 1992. An empirical-model and an inversion technique for radar scattering from bare soil surfaces. IEEE Trans. Geosci. Remote Sens. 30, 370–381.
Pansu, M., Gautheyrou, J., 2006. Handbook of Soil Analysis. Mineralogical, Organic and Inorganic Methods.
Peng, T., Wang, S., 2012. Effects of land use, land cover and rainfall regimes on the surface runoff and soil loss on karst slopes in southwest China. Catena 90, 53–62.
Peng, J., Shen, H., He, S.W., Wu, J.S., 2013. Soil moisture retrieving using hyperspectral data with the application of wavelet analysis. Environ. Earth Sci. 69, 279–288.
Penizek, V., Zadorova, T., Kodesova, R., Vanek, A., 2016. Influence of elevation data resolution on spatial prediction of colluvial soils in a Luvisol region. PLoS One 11, e0165699.
Pineux, N., Lisein, J., Swerts, G., Bielders, C.L., Lejeune, P., Colinet, G., Degré, A., 2017. Can DEM time series produced by UAV be used to quantify diffuse erosion in an agricultural watershed? Geomorphology 280, 122–136.
Raich, J., Tufekcioglu, A., 2000. Vegetation and soil respiration: correlations and controls. Biogeochemistry 48, 71–90.
Ries, F., Lange, J., Schmidt, S., Puhlmann, H., Sauter, M., 2015. Recharge estimation and soil moisture dynamics in a Mediterranean, semi-arid karst region. Hydrol. Earth Syst. Sci. 19, 1439–1456.
Seneviratne, S.I., Corti, T., Davin, E.L., Hirschi, M., Jaeger, E.B., Lehner, I., Orlowsky, B., Teuling, A.J., 2010. Investigating soil moisture-climate interactions in a changing climate: a review. Earth Sci. Rev. 99, 125–161.
Smith, M.P., Zhu, A.X., Burt, J.E., Stiles, C., 2006. The effects of DEM resolution and neighborhood size on digital soil survey. Geoderma 137, 58–69.
Sørensen, R., Seibert, J., 2007. Effects of DEM resolution on the calculation of topographical indices: TWI and its components. J. Hydrol. 347, 79–89.
Suwandana, E., Kawamura, K., Sakuno, Y., Kustiyanto, E., Raharjo, B., 2012. Evaluation of ASTER GDEM2 in comparison with GDEM1, SRTM DEM and topographic-map-derived DEM using inundation area analysis and RTK-dGPS data. Remote Sens. 4, 2419–2431.
Thomas, I.A., Jordan, P., Shine, O., Fenton, O., Mellander, P.E., Dunlop, P., Murphy, P.N.C., 2017. Defining optimal DEM resolutions and point densities for modelling hydrologically sensitive areas in agricultural catchments dominated by microtopography. Int. J. Appl. Earth Obs. Geoinf. 54, 38–52.
Thompson, J.A., Bell, J.C., Butler, C.A., 2000. Digital elevation model resolution: effects on terrain attribute calculation and quantitative soil-landscape modeling. Geoderma 100, 67–89.
Tong, X., Brandt, M., Yue, Y., Horion, S., Wang, K., Keersmaecker, W.D., Tian, F., Schurgers, G., Xiao, X., Luo, Y., Chen, C., Myneni, R., Shi, Z., Chen, H., Fensholt, R., 2018. Increased vegetation growth and carbon stock in China karst via ecological engineering. Nat. Sustain. 1, 44–50.
Umetrics, A.B., 2012. User Guide to SIMCA-P 13.0. Umetrics Inc., Kinnelon.
Unger, P.W., Kaspar, T.C., 1994. Soil compaction and root-growth - a review. Agron. J. 86, 759–766.
Vinzi, V.E., Chin, W.W., Henseler, J., Wang, H., 2010. Handbook of Partial Least Squares (PLS): Concepts, Methods and Applications. Springer-Verlag, Berlin Heidelberg.
Vivoni, E.R., Gebremichael, M., Watts, C.J., Bindlish, R., Jackson, T.J., 2008a. Comparison of ground-based and remotely-sensed surface soil moisture estimates over complex terrain during SMEX04. Remote Sens. Environ. 112, 314–325.
Vivoni, E.R., Rinehart, A.J., Mendez-Barroso, L.A., Aragon, C.A., Bisht, G., Cardenas, M.B., Engle, E., Forman, B.A., Frisbee, M.D., Gutierrez-Jurado, H.A., Hong, S.-h., Mahmood, T.H., Tai, K., Wyckoff, R.L., 2008b. Vegetation controls on soil moisture distribution in the Valles Caldera, New Mexico, during the North American monsoon. Ecohydrology 1, 225–238.
Wagner, W., Scipal, K., Pathe, C., 2003. Evaluation of the agreement between the first global remotely sensed soil moisture data with model and precipitation data. J. Geophys. Res. 108.
White, W.B., 2002. Karst hydrology: recent developments and open questions. Eng. Geol. 65, 85–105.
Wigneron, J.-P., Calvet, J.-C., Pellarin, T., Griend, A.A.V.d., Berger, M., Ferrazzoli, P., 2003. Retrieving near-surface soil moisture from microwave radiometric observations: current status and future plans. Remote Sens. Environ. 85, 489–506.
Wilkinson, M.W., Jones, R.R., Woods, C.E., Gilment, S.R., McCaffrey, K.J.W., Kokkalas, S., Long, J.J., 2016. A comparison of terrestrial laser scanning and structure-from-

motion photogrammetry as methods for digital outcrop acquisition. Geosphere 12, 1865–1880.
Wilson, D.J., Western, A.W., Grayson, R.B., 2005. A terrain and data-based method for generating the spatial distribution of soil moisture. Adv. Water Resour. 28, 43–54.
Wold, S., Sjöström, M., Eriksson, L., 2001. PLS-regression: a basic tool of chemometrics. Chemom. Intell. Lab. Syst. 58, 109–130.
Woodrow, K., Lindsay, J.B., Berg, A.A., 2016. Evaluating DEM conditioning techniques, elevation source data, and grid resolution for field-scale hydrological parameter extraction. J. Hydrol. 540, 1022–1029.
Xu, D.D., Guo, X.L., Li, Z.Q., Yang, X.H., Han, Y., 2014. Measuring the dead component of mixed grassland with Landsat imagery. Remote Sens. Environ. 142, 33–43.
Zhang, J., Chen, H., Su, Y., Shi, Y., Zhang, W., Kong, X., 2011. Spatial variability of surface soil moisture in a depression area of karst region. Clean: Soil Air Water 39, 619–625.
Zhang, Z., Chen, X., Huang, Y., Zhang, Y., 2014. Effect of catchment properties on runoff coefficient in a karst area of southwest China. Hydrol. Process. 28, 3691–3702.
Zhang, T., Peng, J., Liang, W., Yang, Y., Liu, Y., 2016. Spatial-temporal patterns of water use efficiency and climate controls in China's Loess Plateau during 2000–2010. Sci. Total Environ. 565, 105–122.